

RESEARCH ARTICLE | FEBRUARY 08 2019

Modulating near-field heat transfer using oxygen-contaminated piezoelectric aluminum nitride nanomaterials



R. Baltaji; M. Kazan



J. Appl. Phys. 125, 065102 (2019)

<https://doi.org/10.1063/1.5067244>



Boost Your Optics and Photonics Measurements

Lock-in Amplifier

Zurich Instruments

Find out more

Boxcar Averager

Modulating near-field heat transfer using oxygen-contaminated piezoelectric aluminum nitride nanomaterials

Cite as: J. Appl. Phys. **125**, 065102 (2019); doi: [10.1063/1.5067244](https://doi.org/10.1063/1.5067244)

Submitted: 16 October 2018 · Accepted: 21 January 2019 ·

Published Online: 8 February 2019



View Online



Export Citation



CrossMark

R. Baltaji and M. Kazan^{a)}

AFFILIATIONS

Department of Physics, American University of Beirut, P.O. Box 11-0236, Riad El-Solh, Beirut 1107-2020, Lebanon

^{a)}Author to whom correspondence should be addressed: mk140@aub.edu.lb

ABSTRACT

We investigate the modulation of near-field heat transfer between piezoelectric aluminum nitride thin plates and nanospheres. Temperature-dependent infrared spectroscopic measurements showed soft phonon modes indicating a sharp change in the atomic structures of defect complexes in aluminum nitride at a transition temperature. The analysis of the measured infrared spectra showed a drastic change in the infrared dielectric properties upon switching between the observed defect complexes. By using the dielectric properties obtained from measurements, we demonstrate theoretically that the radiative heat transfer between aluminum nitride nanospheres can be dynamically modulated with a peak-to-peak value ranging from 0% to 40% of the maximum net heat transfer upon switching between the atomic structures of defect complexes. The high piezoelectric properties of aluminum nitride materials allow imitating the observed effect of thermal stresses by mechanical stresses resulting from the application of an external electric field.

Published under license by AIP Publishing. <https://doi.org/10.1063/1.5067244>

I. INTRODUCTION

The control of electric currents in solids is at the cornerstone of modern electronics. The electronic components are the fundamental building blocks of modern electronic technologies, enabling rectifying, switching, modulating, and amplifying electric currents. However, the efficiency of the electronic components in harsh environments such as elevated temperatures is poor. The thermal analog of the electronic systems would exhibit better performance and responses in harsh environments, and consequently would pave the way for the new generation of technologies for applications in environments, where the use of the conventional electronic components is very limited. Therefore, much attention has been directed toward thermal structures permitting the control of heat flux.¹⁻⁵ Phononic crystals have been proposed as a potential candidate for thermal technological devices.⁶⁻¹⁰ However, the phonon heat transport is relatively slow as the acoustic phonon's speed is of the order of the speed of sound in solids, and the phonon lifetime is extremely short in high temperature environments. Another limitation is the presence of Kapitza

resistance between different solid elements in contact. All these constraints would drastically reduce the heat flux transported across the phononic system.¹¹ Therefore, an alternative for phononic heat transfer is required to efficiently replace the conventional electronic systems, especially in high temperature environments. Thermal radiation was not habitually considered as an efficient means for thermal management because of its low heat flux in comparison to other heat transfer modes. Nevertheless, with the orders of magnitude enhancement demonstrated in the near-field limit, the near-field radiative heat transfer has shown great potential in the energy transfer at the nanoscale. Hence, the control and modulation of the near-field radiative heat transfer can indeed help realizing the desired photonic alternative to the electronic systems.

Photonic systems operating via the near-field radiative heat transfer (such as thermal transistors,¹² thermal rectifiers,¹³ photonic thermal logic gates,¹⁴ and thermal memory¹⁵) have been theoretically proposed as analogs for the electronic systems. In order to modulate radiative heat transfer and

24 April 2024 08:58:52

achieve the functions of the proposed thermal systems, several approaches have been proposed.^{16–20} A major scheme for modulating the near-field heat transfer is by tuning the optical properties of materials in the infrared spectral range. Classes of materials investigated for modulating the near-field radiative heat transfer so far include phase-change materials (PCMs), ferroelectric materials, and chiral materials. Modulating the near-field radiative heat transfer was proposed for chiral materials with magnetoelectric coupling via ultrafast optical pulses²¹ and for ferroelectric materials via an external electric field.²² Borrowing from research on modulating Casimir force, PCMs such as silver indium antimony tellurite (also known as AIST) and vanadium dioxide (VO₂) have been proposed for modulating the near-field radiative heat transfer.^{23,24} Both can be switched between an amorphous and a crystalline phase with a switching time of the order of a few nanoseconds by changing the material's temperature. Although these materials showed efficient thermal modulation, they are limited to applications in which the temperature does not exceed the critical temperature at which the phase change takes place.

In this paper, we demonstrate experimentally that by changing the lattice parameter of oxygen-contaminated aluminum nitride (AlN), one can tune the atomic configurations of defect complexes, and consequently the material infrared dielectric function, and modulate the near-field radiative heat transfer between AlN nanomaterials. The key advantage of AlN over the conventional PCMs is that it is characterized by high piezoelectric properties, which allow controlling the lattice parameter through the external electric field irrespective of the ambient temperature. In other words, AlN has the advantage that it can be used for modulating the near-field radiative heat transport at temperatures where the conventional PCMs fail. Furthermore, it has been previously established that the two-sphere geometry provides distinctive properties for thermal rectification,²⁵ and the orientation of anisotropic particle system can have a remarkable effect on the near-field interaction between the constituent particles.²⁶ However, modulating the near-field radiative heat transfer by harnessing the properties of phase-change materials has not yet been applied to the two-sphere system. In this paper, we also tackle this issue and demonstrate that the two-sphere geometry has an additional length parameter for heat transfer, thus leading to novel properties for the near-field radiative heat transfer modulation such as controlling dynamically the modulation amplitude.

This paper is structured as follows. After the introduction, we present in Sec. II the sample preparation and infrared measurement procedures. In Sec. III, we present the low temperature reflectivity measurements. We demonstrate that the defect state change occurs in AlN upon varying the lattice parameter. We also demonstrate that the change in the defect state leads to drastic changes in the infrared dielectric function. Using the fluctuational electrodynamics formulation of thermal radiation,²⁷ we investigate the near-field thermal transfer between AlN plates and spheres harnessing the defect state change in AlN for the near-field radiative heat transfer modulation. In Sec. IV, we summarize the results and

conclude with the importance of piezoelectric materials in modulating the near-field radiative heat transfer.

II. EXPERIMENTS

The AlN bulk material investigated in this work was grown by sublimation of an AlN charge placed in the hot zone of a tungsten crucible and subsequent condensation of vapor species in a cooler region. Before the crystal growth, moisture was removed from AlN commercial powder by heating under a vacuum of 10⁻⁷ mbar. Then, AlN powder was resublimed in the growth furnace in the atmosphere of high-purity nitrogen. The powder was kept at 2325 °C and the crucible lid where the material condenses was kept at 2100 °C. Then, the obtained bulk product was placed at the bottom of the tungsten crucible to initiate the growth process. The growth temperature on the crucible lid was set at 2125 °C, and the source temperature was set at 2200 °C. The furnace was operated in high-purity nitrogen gas at a pressure of 900 mbar. A polycrystalline boule of diameter of 2 in. and a height of 10 mm was produced. The sample investigated in this work was obtained from the grown boule. It was formed of crystals of about 1 mm size. Further details about the material growth procedure can be found in Refs. 28 and 29.

Infrared reflectivity measurements were performed in vacuum in the 60–6000 cm⁻¹ frequency range. A 6 μm/Germanium beam splitter and a bolometer were used in the 60–350 cm⁻¹ frequency range, while a potassium bromide (KBr) beam splitter and a nitrogen-cooled deuterated triglycine sulfate (DTGS) detector were used in the 350–6000 cm⁻¹ with a spectral resolution better than 1 cm⁻¹. Energy-dispersion X-ray spectroscopy measurements indicated that oxygen is the dominant impurity in the sample, and glow discharge mass spectroscopy (GDMS) on polycrystalline rods of 2 × 2 × 20 mm³ size cut from the sample investigated indicated that oxygen is present in this sample at a concentration of approximately 1 at. %. High-quality surface was prepared by polishing the sample surface in a non-aqueous medium containing a mixture of hydrogen fluoride and ammonium fluoride immediately prior to the infrared spectroscopic analysis to avoid contribution from oxide layers formed on the sample surface. The root mean square (rms) roughness of the sample surface was too small to have any contribution to the measured spectra (about a few nanometers). The infrared reflectivity spectra were recorded for near-normal incidence and unpolarized light. An infrared cryostat was used to vary the sample temperature from 10 K to room temperature.

III. RESULTS AND DISCUSSION

Oxygen-related defect complexes have always been considered as the most important native defects in AlN ceramics. Their local atomic structure has been intensively investigated.^{30–33} Theories have shown that oxygen acts as a deep center in the wide electronic bandgap of AlN and substitutes for the nitrogen atom in several charge states. Experiments demonstrated that a change in the nature of oxygen-related defect complexes occurs above a critical

value of oxygen concentration.^{34,35} It has been suggested that at concentrations below 0.75%, oxygen substitutes for nitrogen in the lattice with one aluminum vacancy occurring for every three substituted oxygen atoms, and for a concentration greater than 0.75%, a new type of defect is stable in which an aluminum atom octahedrally bounds to an increasing number of oxygen atoms. However, no effect of stress on defect complexes has been reported.

Despite the substantial uncertainty about the exact atomic configurations of oxygen-related defect complexes in AlN, the contribution of their vibrational modes to the reststrahlen infrared band can somehow be predicted. In fact, the wurtzite structure of AlN belongs to the space group C_{6v}^4 with two Al atoms and two N atoms occupying C_{3v} sites in one unit cell. The phonon dispersion curves of such a structure are characterized by an extremely small energy gap between the acoustic and optical phonon bands.^{36,37} Hence, any impurity with an atomic mass larger than that of nitrogen substituting for nitrogen would give rise to an in-band resonance mode and distort significantly the reststrahlen band of the AlN lattice.³² Therefore, we have traced the effect of thermal stress on defect complexes in AlN through their vibrational modes using temperature-dependent infrared spectroscopy. We have applied a compressive thermal stress by lowering the temperature of the measured sample. We found that between 300 and 90 K, all the infrared reflectivity spectra exhibit the same features, indicating stable defect complexes in this temperature range. However, we observed a clear transference in the atomic structures of defect complexes when the temperatures go below 90 K. The reflectivity measurements revealed localized phonon resonance modes at 390 and 445 cm^{-1} and an in-optical-band resonance mode at 660 cm^{-1} . On the other hand, below 90 K, the resonance mode at 390 cm^{-1} vanishes and the resonance modes at 445 cm^{-1} and 660 cm^{-1} enhance significantly. We illustrate the results of the infrared reflectivity measurements in Fig. 1. We show infrared reflectivity spectra recorded at 300 K and 70 K. These spectra clearly demonstrate different atomic configurations of defect complexes. The inset figure shows a clear atomic configuration transition occurring when the temperature goes below 90 K. We refer to the defect state occurring at high temperatures as “High-T-State” and that occurring below 90 K as “Low-T-State.” Since for oxygen concentration greater than 0.75% a stable defect complex forms, we expect that the change in the defect state observed in the sample investigated upon the application of a compressive stress would occur in any AlN crystal of oxygen concentration greater than 0.75%.

We have used the Kramers-Kronig theorem to convert the measured reflectivity data into dielectric properties. It is worth noting here that the measurement of the reflectivity spectra from a very low frequency up to a frequency at which the derivative of the infrared reflectivity with respect to frequency vanishes allows highly accurate Kramers-Kronig conversion. In Fig. 2, we illustrate the real and imaginary parts of the dielectric function as derived from the reflectivity spectra measured at 300 K and at 70 K. We find that upon atomic configuration transition below 90 K, both the real and imaginary

parts of the infrared dielectric function enhance dramatically in the spectral region of the reststrahlen infrared band, i.e., in the region of the existence of the surface phonon polariton modes, which are the principal determinants of the heat transfer in the near-field limit.^{38–41} A multi-Lorentzian-peak function of the form

$$\epsilon = \gamma_0 + \sum_j \frac{2A_j}{\pi} \frac{\sigma_j}{4(\omega - \omega_{c,j})^2 + \sigma_j^2} \quad (1)$$

is fitted to the obtained real and imaginary parts of the dielectric functions of both High-T-State and Low-T-State. In Eq. (1), ω denotes the measured wavenumbers. The other parameters of the multi-peak fitting that generate the real and imaginary parts of the measured dielectric functions are given in Tables I and II, respectively. In what follows, we investigate the implication of the experimentally observed drastic change in the infrared complex dielectric function on the near-field radiative heat transfer between oxygen-contaminated AlN nanomaterials by using dyadic Green’s functions within the fluctuational electrodynamics formulation of thermal radiation and stochastic Maxwell equations.^{42–47} Because of the high piezoelectric properties of AlN, the change in the defect state observed upon introducing thermal stress can occur at room temperature upon introducing mechanical stress through the application of an external electric field. In fact, upon lowering the temperature from 300 K to 70 K, the AlN lattice contracts in the c -axis direction by $\Delta c/c = \alpha_c(T) \times \Delta T$, where ΔT is the difference between the final temperature and initial temperature

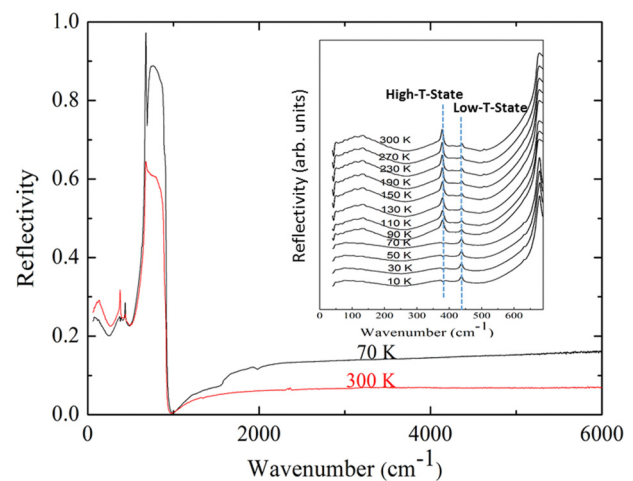


FIG. 1. Temperature-dependent infrared reflectivity spectra. The full reflectivity spectra are shown only for temperatures of 300 and 70 K. The inset figure shows low frequency reflectivity spectra measured at different temperatures. The reflectivity measurements reveal the localized phonon resonance modes at 390 and 445 cm^{-1} and an in-optical-band resonance mode at 660 cm^{-1} . At 70 K and below, the low-frequency reflectivity spectrum changes dramatically indicating a change in the defect state when the temperature goes below 90 K.

24 April 2024 08:58:52

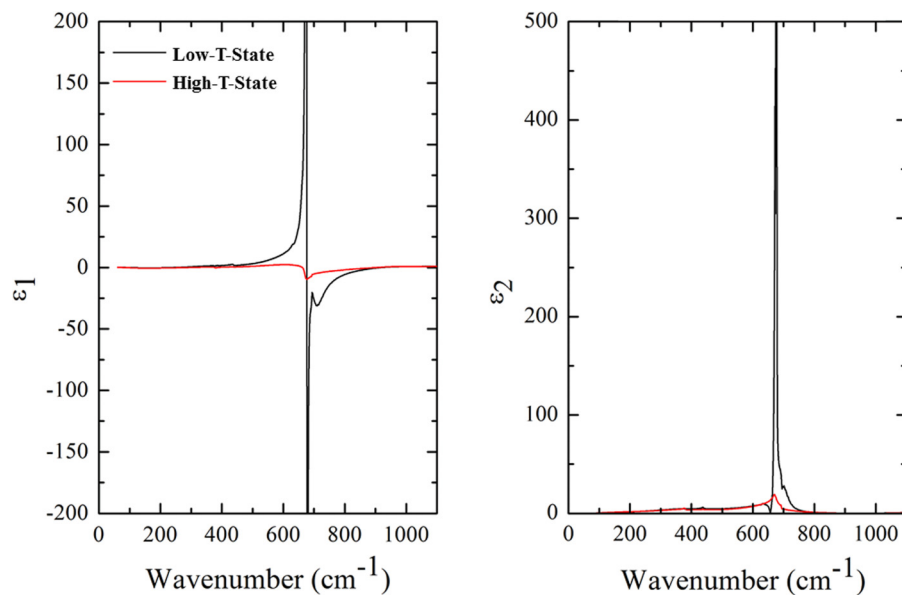


FIG. 2. Real and imaginary parts of the AlN infrared dielectric function for the two observed defect states.

and $\alpha_c(T)$ is the temperature dependent linear thermal expansion of AlN in the c -axis direction.⁴⁸ Such a contraction corresponds to a compressive thermal stress of $S = Y \times \Delta c/c$, where Y is AlN Young's modulus, which is equal to 308 GPa,⁴⁹ and c is the temperature dependent AlN axial lattice constant.⁴⁸ On the other hand, the e_{33} piezoelectric constant of AlN is as large as 1.55 C m^{-2} .⁵⁰ This means that an electric field of the magnitude of $Y \cdot \Delta c/c \cdot e_{33} = Y \cdot \alpha(T) \cdot \Delta T/e_{33} = 3 \times 10^5 \text{ N/C}$ (which is three orders of magnitude smaller than the breakdown field of AlN) directed along the c -axis may produce the same amount of stress on the AlN lattice and tune between the defect states observed in temperature-dependent infrared reflectivity measurements. Therefore, we carry out calculations at room temperature assuming switching between defects states at room temperature by means of mechanical stresses. We explore the parallel-plate and two-sphere geometries.

A. Parallel-plate geometry

For the parallel-plate geometry, we considered plates separated by a vacuum gap of width d . We calculated the spectral and net heat transfer for this geometry using dyadic Green's function in Refs. 51 and 52. In Fig. 3, we illustrate the calculated spectral and net heat transfer at 300 K spanning gaps of several orders of magnitude for both experimentally detected defect states (i.e., using the dielectric functions corresponding to the two detected defect states in AlN). It is clear from the spectral heat transfer plots that in the near field limit, conduction is dominated by surface phonon polariton, which is manifested by maximal radiation at their

resonance frequencies.²⁰ Another interesting phenomenon manifesting itself in the gap-dependent spectral heat transfer plots is that the defect state occurring at low temperatures leads to a more coherent near-field radiative heat transfer. The slope of the curve describing the net heat transfer as a function of the separation gap in a logarithmic plot demonstrates the expected d^{-2} dependence in the near-field regime (i.e., in the region where the separation gap is smaller than the $10 \mu\text{m}$ thermal wavelength). Yet, these results also demonstrate that by tuning between these two experimentally observed defect states, the near-field radiative heat transfer changes by 40% irrespective to the separation gap. Hence, the variation of the separation gap in the two-plate geometry allows controlling the net heat transfer but not the amplitude of the modulation resulting from tuning between the two defect states observed in AlN. Geometries including additional length parameters are therefore required to control the amplitude of the modulation of the near-field radiative heat transfer. The two-sphere geometry includes the two length parameters needed to control the modulation amplitude. These length parameters are the separation gap and the radius of the spheres. Thus, the two-sphere geometry may provide opportunities to control both the magnitude of the net heat transfer and the modulation amplitude upon tuning between the defect states observed in AlN.

B. Two-spheres geometry

We have investigated the near-field radiative heat transfer between identical spheres. For spheres separated by small gaps compared to the spheres radii, an asymptotic expression

24 April 2024 08:58:52

TABLE I. Parameters to generate from [Eq. (1)] the real part of the dielectric function for both High-T-State and Low-T-State.

Defect state	Spectral range (cm ⁻¹)	y ₀	ω _c (cm ⁻¹)	σ (cm ⁻¹)	A (cm ⁻¹)	
High-T-State	60–600	0.41105	136.41464	114.50503	-78.63228	
			217.38867	307.50057	-668.1532	
			380.14928	14.74224	-160.10697	
			381.66021	12.68679	63.48265	
			474.69669	290.58989	-1089.70547	
			378.06933	15.61153	84.47437	
			585.65531	578.3991	3257.62372	
			673.54904	20.81377	-1649.39161	
			597.09679	317.20378	11858.32428	
			672.90602	22.68604	1573.41601	
	600–1000	-31.03822	686.78846	18.75486	-118.63595	
			705.78413	73.06202	-397.92287	
			826.17485	199.84513	679.25045	
			1009.91578	587.76496	25926.50991	
			940.95974	527.99322	-852.87487	
			1304.77869	643.74305	-309.67299	
			2277.3375	1387.01553	703.36826	
			2796.51324	981.62821	407.73074	
			3212.90522	578.91177	148.32177	
			3601.5232	1335.52631	1123.23347	
Low-T-State	60–600	-1.02177	4118.65803	906.4253	788.43616	
			65.11674	127.48052	154.32857	
			412.3652	410.37687	-757.26662	
			358.70194	199.78197	552.46372	
			436.33311	14.0136	85.0035	
			437.73951	15.56946	-87.03353	
			424.82038	39.87706	34.17956	
			679.05417	182.79167	6303.82926	
			675.1403	3.05186	10580.50775	
			683.24434	39.38168	4830.32356	
	600–674	6.18473	677.12876	3.28266	-5639.70045	
			683.48557	5.29912	84.53779	
			711.17813	43.64062	-1210.43098	
			2018.6089	5.65052	3211917.3741	
			1019.10579	241.55338	5064.27439	
			902.97143	201.65401	2656.72639	
			832.2211	125.37403	888.31419	
			792.41631	71.7069	273.82187	
			764.25502	42.36033	74.66619	
			1994.4721	2208.36178	-2964.99141	
674–700	-15.21469	930.74038	762.47501	-4741.34579		
		1370.39507	505.15246	-913.96464		
		1519.14625	137.90288	-88.17053		
		1902.65953	168.87332	578.59788		
		1788.36835	1503.65562	1627.86373		
		1905.13573	201.0595	-767.28524		
		700–1000	-19.95777	1994.4721	2208.36178	-2964.99141
				930.74038	762.47501	-4741.34579
				1370.39507	505.15246	-913.96464
				1519.14625	137.90288	-88.17053
1902.65953	168.87332			578.59788		
1788.36835	1503.65562			1627.86373		
1905.13573	201.0595			-767.28524		
1000–4000	5.1496			930.74038	762.47501	-4741.34579
				1370.39507	505.15246	-913.96464
				1519.14625	137.90288	-88.17053
		1902.65953	168.87332	578.59788		
		1788.36835	1503.65562	1627.86373		
		1905.13573	201.0595	-767.28524		
		1000–4000	5.1496	930.74038	762.47501	-4741.34579
				1370.39507	505.15246	-913.96464
				1519.14625	137.90288	-88.17053
				1902.65953	168.87332	578.59788
1788.36835	1503.65562			1627.86373		
1905.13573	201.0595			-767.28524		

TABLE II. Parameters to generate from [Eq. (1)] the imaginary part of the dielectric function for both High-T-State and Low-T-State.

Defect state	Spectral range (cm ⁻¹)	y ₀	ω _c (cm ⁻¹)	σ (cm ⁻¹)	A (cm ⁻¹)	
High-T-State	60–600	0.8627	52.90643	140.21803	-314.68366	
			386.7189	306.53986	793.30085	
			377.46216	14.16984	57.74765	
			355.24059	110.5036	179.62324	
			381.19041	20.28132	-59.33619	
			436.48334	11.18043	6.24315	
			660.14328	179.17556	2334.05005	
			670.27744	17.21027	264.36632	
			660.10282	101.8138	1638.19783	
			693.25371	8.11926	-266.88946	
	600–1000	-0.35372	489.30258	27.91272	10124.15423	
			697.82607	61.25787	-277.7128	
			931.56917	47.23299	-31.33739	
			692.85816	8.39322	272.53166	
			845.105	38.9942	-2241.98294	
			1020.30545	285.37107	-144.02617	
			2056.48059	1871.34709	557.21422	
			1617.65326	1614.00419	841.20666	
			3428.5823	545.09871	46.38744	
			232.99842	2578.26697	1271.92713	
Low-T-State	60–600	-0.18614	2667.45088	1167.47149	159.75397	
			5320.12779	736.39107	-83974.84399	
			174.77699	351.57706	706.08528	
			396.01414	266.23379	969.84087	
			346.69381	180.07628	413.67682	
			-927.73547	1240.51898	-11308.81534	
			436.16576	9.68852	23.83184	
			761.70959	289.29994	8067.91887	
			674.96378	0.00009	6.1023	
			672.69407	4.80985	3165.41704	
	600–674	4.96669	676.23979	1.30452	6931.41934	
			693.39961	29.01365	1362.80156	
			702.53716	5.38013	29.72994	
			702.54476	12.62494	398.73959	
			721.20568	34.44735	-132.05469	
			691.02386	152.34391	487.6538	
			703.61202	4.93016	-75.22767	
			960.3418	0.0012	-459.31568	
			711.45579	40.17191	817.53499	
			2361.38685	1043.63846	856.25783	
674–700	2.46509	1413.50046	288.26741	311.31577		
		1832.53675	645.93335	801.80455		
		2030.19769	61.26976	-7.33328		
		2913.25856	2266.05145	2382.14158		
		1233.86242	248.24566	270.06665		
		1113.02713	134.2458	63.69811		
		700–1000	-0.23787	702.53716	5.38013	29.72994
				702.54476	12.62494	398.73959
				721.20568	34.44735	-132.05469
				691.02386	152.34391	487.6538
703.61202	4.93016			-75.22767		
960.3418	0.0012			-459.31568		
711.45579	40.17191			817.53499		
2361.38685	1043.63846			856.25783		
1413.50046	288.26741			311.31577		
1832.53675	645.93335			801.80455		

24 April 2024 08:58:52

can be derived from the results of near-field radiative transfer in the two-plate geometry. Such a method, which has been widely used for the calculation of Casimir and Van der Waals forces, is known as the proximity limit theory.⁵³ The proximity limit theory predicts near-field conductance varying linearly with d/r for spheres smaller than the radiation wavelength and separated by small gaps ($d \ll r < \lambda$).²⁷ On the other hand, very small spheres of radii much smaller than the thermal wavelength can be treated as point dipoles. In that case, the

conductance between the spheres is given by the dipole approximation,⁵⁴ which predicts a near-field conductance varying as $1/d^6$. In order to investigate wide ranges of both length parameters characterizing the two-sphere geometry, we have calculated the spectral and total conductance between two identical AlN nanospheres using dyadic Green's functions of the vector Helmholtz equation in spherical coordinates within the fluctuational electrodynamics framework.²⁷ This calculation method is applicable to any spheres radius

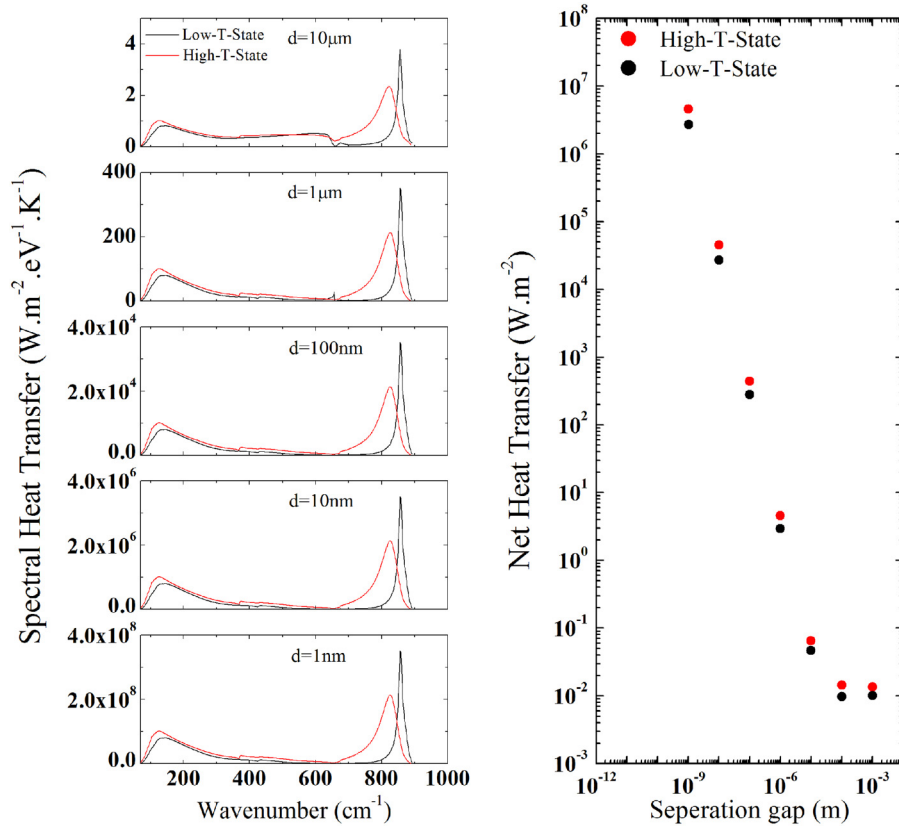


FIG. 3. Spectral and net heat transfer between AlN parallel plates as a function of the separation gap for the two observed defect states. Red solid lines and symbols correspond to the defect state occurring at high temperatures. Black solid lines and symbols correspond to the defect state occurring at low temperatures.

24 April 2024 08:58:52

and separation gap. We spanned gaps and radii of several orders of magnitude for both defect states observed in AlN. Similar to the two-plate geometry, the spectral conductance for all the investigated combinations of radius and separation gap show that the conduction is dominant by surface phonon polariton, and the coherence of the near-field radiation enhances when tuning the defect state from “High-T-State” to “Low-T-State.” In Fig. 4, we illustrate the spectral and total conductance calculated for different radii and gaps and for both defect states observed in AlN. Here, the spectral conductance values are calculated with involving different radii and gaps, while maintaining a constant radius to gap ratio. The spectral conductance calculation results show for larger radii a well-pronounced contribution of propagating non-resonant modes to the total heat transfer, which can potentially swamp the resonant near-field radiative transfer.²⁷ Furthermore, the total conductance calculated as a function of spheres radius and separation gap clearly shows the transition between the $1/d^6$ dependence predicted by the dipole approximation and the d/r dependence predicted by the proximity limit theory.

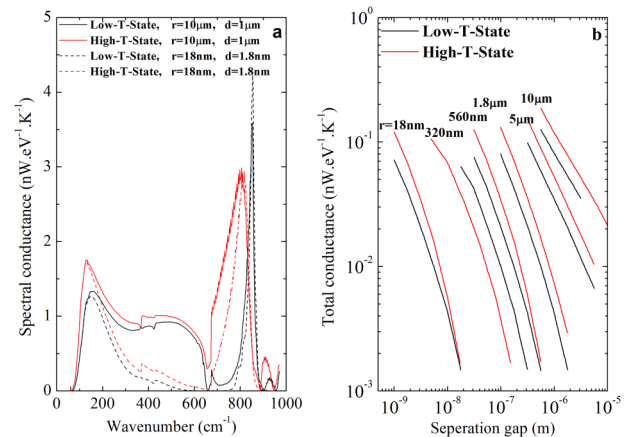


FIG. 4. Spectral and net heat transfer between two identical spheres of AlN as functions of the separation gap and spheres radius. Dashed and solid red lines correspond to the defect state occurring at high temperatures. Dashed and solid black lines correspond to the defect state observed at low temperatures.

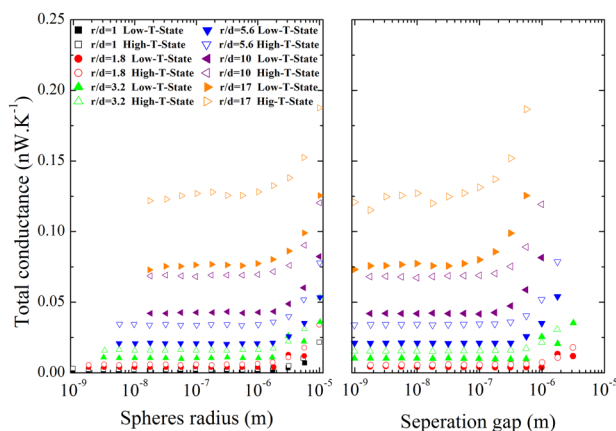


FIG. 5. Variation of the total conductance with sphere radius and separation gap. Each symbol corresponds to a constant radius to gap ratio. Open symbols correspond to the defect state occurring at high temperatures. Closed symbols correspond to the defect state occurring at low temperatures. The difference between the open and closed symbols indicates the amplitude of the modulation of the near-field radiative heat transfer. Calculations were done until convergence to the limit of parallel plates was observed.

The question that comes up here is whether it is possible to use the additional length parameter of the two-sphere geometry to control the modulation amplitude upon tuning between the two defect states observed in AlN. In order to answer this question, we have calculated the total conductance between two identical nanospheres in wide ranges of radius and separation gap for different radius to gap ratios and for both defect states of AlN. The results are shown in Fig. 5. The total conductance as a function of radius to gap ratio for both High-T-State and Low-T-State is shown in Fig. 6. The results illustrated in Figs. 5 and 6 demonstrate that in the near-field limit, the total conductance is determined by only the radius to gap ratio and increases as the radius to gap ratio increases due to propagating non-resonant modes whose contribution to the heat transfer increases as the spheres radius increases, which agrees with previous calculations.²⁷ However, the key development presented in these results is that the change in total conductance upon tuning between the defect states observed in AlN increases consistently with increasing the radius to gap ratio. They show a negligible change for a radius to gap ratio of one, and a change of 40% for a radius to gap ratio of 17, for which the two-sphere geometry approaches the limit of the two-plate geometry. These results therefore strongly suggest the use of AlN nanospheres for modulating the near-field radiative heat transfer and controlling dynamically the modulation amplitude between 0% and 40% for controlling the power of thermal loads on the thermal analog of the electronic systems as well as for many applications involving efficient nanoscale energy transfer.

We note here that the results presented in this section for the parallel-plate and two-sphere geometries are obtained under the assumption that the surfaces of the plates and

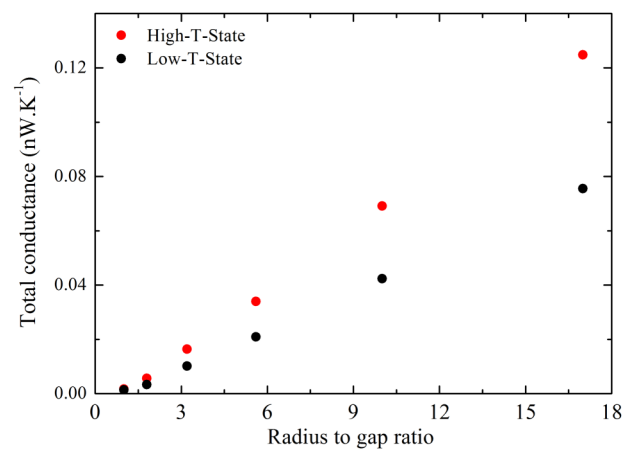


FIG. 6. Total thermal conductance between two identical spheres of AlN as a function of radius to gap ratio for both experimentally detected defect states. Red symbols correspond to the defect state occurring at high temperatures. Black symbols correspond to the defect state occurring at low temperatures.

spheres are perfectly smooth. In the case of the presence of surface roughness, experiments demonstrated that the near-field radiative heat transfer is significantly different from that between two perfectly smooth surfaces.^{55–58} The numerical approach employed in the present work is not suitable for predicting the effect of surface roughness on near-field radiative heat transport. However, theoretical investigations using the proximity approximation demonstrated that for parallel plates satisfying the proximity conditions, scattering of surface modes on only one rough plate surface leads to an appreciable decrease in the heat flux,⁵⁹ whereas scattering of surface modes on both surfaces by roughness causes a larger heat flux.⁶⁰ On the other hand, the finite-difference time-domain (FDTD) method with the Weiner Chaos Expansion method showed that the near-field radiative heat transfer might be decreased by very small surface roughness.⁶¹ For the case of curved surfaces such as spheres, it was demonstrated that the surface roughness leads to an appreciable modification in the well-established scaling law,⁶² which is illustrated here in Fig. 4.

IV. CONCLUSION

Temperature-dependent infrared reflectivity measurements in the far- and mid-infrared demonstrated that upon the application of a thermal strain, changes in the defect states occur in oxygen contaminated aluminum nitride. The analysis of the measured spectra using the Kramers-Kronig theorem showed that the observed changes in the defect states lead to strong changes in the material complex infrared dielectric function. These observations motivated us to investigate the implications of the alteration in the infrared dielectric properties on the near-field radiative heat transfer between parallel plates and identical nanospheres of oxygen

24 April 2024 08:58:52

contaminated aluminum nitride. We demonstrated theoretically the possibility of significantly modulating the near-field radiative heat transfer and controlling the modulation amplitude in the two-sphere system via harnessing the drastic changes in the infrared complex dielectric function of the emitters. In our calculation, we adopted the fluctuational electrodynamics formulation of thermal radiation and stochastic Maxwell equations. We showed that the two-sphere configuration allows modulating the near-field radiative heat transfer through tuning between the experimentally observed defect states in aluminum nitride and offers the opportunity of dynamically controlling the modulation amplitude from 0% to 40% through tuning the radius to gap ratio. The high piezoelectric properties of aluminum nitride render the possibility of applying mechanical strains on the aluminum nitride lattice by the application of an external electric field, and consequently imitating the effect of thermal strain and modulating the near-field radiative heat transfer at any temperature.

ACKNOWLEDGMENTS

The authors would like to acknowledge the financial support by Munib and Angela Masri Institute of Energy and Natural Resources and the American University of Beirut Research Board (URB).

REFERENCES

- ¹D. G. Cahill, W. K. Ford, K. E. Goodson, G. D. Mahan, A. Majumdar, H. J. Maris, R. Merlin, and S. R. Phillpot, *J. Appl. Phys.* **93**, 793 (2003).
- ²S. Basu and Z. M. Zhang, *J. Appl. Phys.* **105**, 093535 (2009).
- ³A. D. Phan, T.-L. Phan, and L. M. Woods, *J. Appl. Phys.* **114**, 214306 (2013).
- ⁴J. Y. Chang, S. Basu, Y. Yang, and L. Wang, *J. Appl. Phys.* **119**, 213108 (2016).
- ⁵T. Ikeda, K. Ito, and H. Lizuka, *J. Appl. Phys.* **121**, 013106 (2017).
- ⁶B. L. Davis and M. I. Hussein, *Phys. Rev. Lett.* **112**, 055505 (2014).
- ⁷L. Yang, N. Yang, and B. W. Li, *Nano Lett.* **14**, 1734 (2014).
- ⁸N. Zen, T. A. Puurtinen, T. J. Isotalo, S. Chaudhuri, and I. J. Maasilta, *Nat. Commun.* **5**, 3435 (2014).
- ⁹H. Nonarvar and M. I. Hussein, *Phys. Rev. B* **93**, 054109 (2016).
- ¹⁰A. Iskandar, A. Gwiazda, Y. Huang, M. Kazan, A. Bruyant, M. Tabbal, and G. Lerondel, *J. Appl. Phys.* **120**, 095106 (2016).
- ¹¹P. Ben-Abdallah and S.-A. Biehs, *Z. Naturforsch. A* **72**(2), 151 (2017).
- ¹²P. Ben-Abdallah and S.-A. Biehs, *Phys. Rev. Lett.* **112**, 044301 (2014).
- ¹³C. R. Otey, W. T. Lau, and S. Fan, *Phys. Rev. Lett.* **104**, 154301 (2010).
- ¹⁴P. Ben-Abdallah and S.-A. Biehs, *Phys. Rev. B* **94**, 241401 (2016).
- ¹⁵V. Kubyt'skiy, S.-A. Biehs, and P. Ben-Abdallah, *Phys. Rev. Lett.* **113**, 074301 (2014).
- ¹⁶S.-A. Biehs, F. S. Rosa, and P. Ben-Abdallah, *Appl. Phys. Lett.* **98**, 243102 (2011).
- ¹⁷A. W. Rodriguez, M. T. H. Reid, and S. G. Johnson, *Phys. Rev. B* **86**, 220302 (2012).
- ¹⁸A. I. Volokitin and B. N. J. Persson, *Phys. Rev. B* **78**, 155437 (2008).
- ¹⁹G. Dedkov and A. Kyasov, *Surf. Sci.* **604**, 562 (2010).
- ²⁰H. Karakachian and M. Kazan, *J. Appl. Phys.* **122**, 045103 (2017).
- ²¹L. Cui, Y. Huang, and J. Wang, *J. Appl. Phys.* **112**, 084309 (2012).
- ²²Y. Huang, S. V. Boriskina, and G. Chen, *Appl. Phys. Lett.* **105**, 244102 (2014).
- ²³P. Van Zwol, K. Joulain, P. B. Abdallah, J.-J. Greffet, and J. Chevrier, *Phys. Rev. B* **83**, 201404 (2011).
- ²⁴P. Van Zwol, K. Joulain, P. B. Abdallah, and J. Chevrier, *Phys. Rev. B* **84**, 161413 (2011).
- ²⁵L. Zhu, C. R. Otey, and S. Fan, *Phys. Rev. B* **88**, 184301 (2013).
- ²⁶M. Nikbakht, *J. Appl. Phys.* **116**, 094307 (2014).
- ²⁷A. Narayanaswamy and G. Chen, *Phys. Rev. B* **77**, 075125 (2008).
- ²⁸B. M. Epelbaum, M. Bickermann, and A. Winnacker, *J. Cryst. Growth* **269**, 432 (2004).
- ²⁹M. Bickermann, B. M. Epelbaum, M. Kazan, Z. Herro, P. Masri, and A. Winnacker, *Phys. Status Solidi (a) Appl. Mater. Sci.* **202**, 531 (2005).
- ³⁰T. Mattila and R. M. Nieminen, *Phys. Rev. B* **54**, 16676 (1996).
- ³¹Q. Hu, T. Noda, H. Tanigawa, T. Yoneoka, and S. Tanaka, *Nucl. Instrum. Methods Phys. Res. Sect. B Beam Interact. Mater. Atoms* **191**, 536 (2002).
- ³²M. Kazan, B. Rufflé, C. Zgheib, and P. Masri, *J. Appl. Phys.* **98**, 103529 (2005).
- ³³M. A. Signore, M. A. Taurino, D. Valerini, A. Rizzo, I. Farella, M. Catalano, F. Quaranta, and P. Siciliano, *J. Alloys Compd.* **649**, 1267 (2015).
- ³⁴R. A. Youngman and J. H. Harris, *J. Am. Ceram. Soc.* **73**, 3238 (1990).
- ³⁵L. E. McNeil, M. Grimsditch, and R. H. French, *J. Am. Ceram. Soc.* **76**, 1132 (1993).
- ³⁶H. M. Tütüçü and G. P. Srivastava, *Phys. Rev. B* **62**, 5028 (2000).
- ³⁷V. Y. Davydov, Y. E. Kitaev, I. N. Goncharuk, A. N. Smirnov, J. Graul, O. Semchinova, D. Uffmann, M. B. Smirnov, A. P. Mirgorodsky, and R. A. Evarestov, *Phys. Rev. B* **58**, 12899 (1998).
- ³⁸Y. De Wilde, F. Formanek, R. Carminati, B. Gralak, P.-A. Lemoine, K. Joulain, J.-P. Mulet, Y. Chen, and J.-J. Greffet, *Nature* **444**, 740 (2006).
- ³⁹J. D. Caldwell, L. Lindsay, V. Giannini, I. Vurgaftman, T. L. Reinecke, S. A. Maier, and O. J. Glembocki, *Nanophotonics* **4**, 44 (2015).
- ⁴⁰J. D. Caldwell, O. J. Glembocki, Y. Francescato, N. Sharac, V. Giannini, F. J. Bezares, J. P. Long, J. C. Owrutsky, I. Vurgaftman, J. G. Tischler, V. D. Wheelert, N. D. Bassim, L. M. Shirey, R. Kasica, and S. A. Maier, *Nano Lett.* **13**, 3690 (2013).
- ⁴¹J.-J. Greffet, R. Carminati, K. Joulain, I.-P. Mulet, S. Mainguy, and Y. Chen, *Nature* **416**, 61 (2002).
- ⁴²J. D. Jackson, *Classical Electrodynamics* (Wiley, 1999).
- ⁴³M. Francoeur and M. P. Mengüç, *J. Quant. Spectrosc. Radiat. Transf.* **109**, 280 (2008).
- ⁴⁴G. Kristensson, *Scattering of Electromagnetic Waves by Obstacles* (The Institution of Engineering and Technology, 2016).
- ⁴⁵L. D. Landau, J. Bell, M. Kearsley, L. Pitaevskii, E. Lifshitz, and J. Sykes, *Electrodynamics of Continuous Media* (Elsevier, 2013), Vol. 8.
- ⁴⁶K. Joulain, R. Carminati, J.-P. Mulet, and J.-J. Greffet, *Phys. Rev. B* **68**, 245405 (2003).
- ⁴⁷M. Francoeur, *Near-Field Radiative Transfer: Thermal Radiation, Thermophotovoltaic Power Generation and Optical Characterization* (University of Kentucky, 2010).
- ⁴⁸H. Kröncke, S. Figge, B. M. Epelbaum, and D. Hommel, *Acta Phys. Pol. A* **114**, 1193 (2008).
- ⁴⁹D. Gerlich, S. L. Dole, and G. A. Slack, *J. Phys. Chem. Solids* **47**, 437 (1986).
- ⁵⁰Y. Goldberg, in *Properties of Advanced Semiconductor Materials GaN, AlN, InN, BN, SiC, SiGe*, edited by M. E. Levinstein, S. L. Rumyantsev, and M. S. Shur (John Wiley & Sons, Inc., New York, 2001).
- ⁵¹K. Joulain, J.-P. Mulet, F. Marquier, R. Carminati, and J.-J. Greffet, *Surf. Sci. Rep.* **57**, 59 (2005).
- ⁵²C. Fu and Z. Zhang, *Int. J. Heat Mass Transf.* **49**, 1703 (2006).
- ⁵³J. Blocki, J. Randrup, W. Świątecki, and C. Tsang, *Ann. Phys. (N.Y.)* **105**, 427 (1977).
- ⁵⁴G. Domingues, S. Volz, K. Joulain, and J.-J. Greffet, *Phys. Rev. Lett.* **94**, 085901 (2005).
- ⁵⁵L. Hu, A. Narayanaswamy, X. Chen, and G. Chen, *Appl. Phys. Lett.* **92**, 133106 (2008).
- ⁵⁶A. Narayanaswamy, S. Shen, and G. Chen, *Phys. Rev. B* **78**, 115303 (2008).
- ⁵⁷S. Shen, A. Narayanaswamy, and G. Chen, *Nano Lett.* **9**, 2909 (2009).
- ⁵⁸E. Rousseau, A. Siria, G. Jourdan, S. Volz, F. Comin, J. Chevrier, and J.-J. Greffet, *Nat. Photonics* **3**, 514 (2009).
- ⁵⁹S.-A. Biehs and J.-J. Greffet, *Phys. Rev. B* **81**, 245414 (2010).
- ⁶⁰S.-A. Biehs and J.-J. Greffet, *Phys. Rev. B* **82**, 245410 (2010).
- ⁶¹Y. Chen and Y. Xuan, *J. Quant. Spectrosc. Radiat. Transf.* **158**, 52 (2015).
- ⁶²M. Kruger, V. A. Golyk, G. Bimonte, and M. Kardar, *EPL* **104**, 41001 (2013).